

Scaling of Time-Dependent Tunneling Current in Terahertz Scanning Tunneling Microscopes

Sneha Banerjee^{ID, †, ‡} and Peng Zhang^{ID, *}

Department of Electrical and Computer Engineering, Michigan State University, East Lansing, Michigan 48824, USA



(Received 21 March 2022; revised 8 June 2022; accepted 15 July 2022; published 3 August 2022)

Terahertz scanning tunneling microscopy (THz-STM) has enabled spatiotemporal imaging with femtosecond temporal resolution and angstrom spatial resolution. In THz-STMs, the junction bias is modulated by coupling THz pulses, which results in transient voltage bias and extremely high transient tunneling currents. In order to have efficient imaging of the sample surface, it is important to understand the nonlinear tunneling current response and its parametric dependence. In this work, we theoretically investigate the basic scaling of rectified electrons in a THz-STM junction. We use a self-consistent quantum model that includes both space-charge potential and exchange-correlation potential, which were ignored in previous studies. Since THz-STMs are operated at high transient voltage in field emission regime, the effects of exchange-correlation potential become crucial. We validate our calculation with recently reported experimental data and investigate the rectification property of the tip-sample junction for different parameters. We find that the time-dependent tunneling current and the electron transport can be manipulated by varying the dc bias voltage (polarity, amplitude), incident THz field (polarity, shape, peak amplitude), work functions of STM tip and sample—especially their difference ΔW , and the tip-sample separation. Our study provides an important framework that can be used in the future to characterize, control, and improve THz-induced currents and probing techniques at the nanometer scale over subpicosecond time periods.

DOI: 10.1103/PhysRevApplied.18.024011

I. INTRODUCTION

A scanning tunneling microscope (STM) is an instrument that uses the quantum tunneling [1] phenomenon for imaging surfaces at the atomic level [2–5]. In order to observe and record the time dynamics of microscopic structures [6–8], STMs must have ultrafast temporal resolution [9–12] and atomic spatial resolution. Efforts have been made to integrate femtosecond lasers with STMs to improve temporal resolution [13,14]. These methods offer time resolution up to approximately 10 ps for nanometer spatial resolution [15] and they need specialized probe or sample structures [15]. In 2013 Cocker *et al.* [9] showed that the time resolution can be improved to the subpicosecond level with atomic spatial resolution [8,9,16] by modulating the STM junction bias directly with terahertz (THz) pulses focused on the scanning probe tip. Experiments show that tunneling currents at a milliamp scale can be achieved over ultrafast time scales without damaging the STM tip or sample [9,16–18], which is not typically possible in conventional STMs.

In THz-STMs, free-space-traveling terahertz pulses, which are polarized parallel to the STM tip (i.e., the direction of the electric field is in alignment with the tip) [9], are focused onto the scanning probe tip [Fig. 1(a)]. The STM tip acts like a broadband antenna [19,20] and couples the electric field of the incident THz pulses to the tip-vacuum-sample junction. It uses the nonlinear current-voltage ($I - V$) behavior of the tunnel junction to produce a rectified ultrafast current burst [9]. Experiments [8,9,17,18,21,22] showed that peak THz voltage bias transients greater than 3 V across the STM junction can be achieved leading to field emission of subpicosecond tunnel currents with current densities exceeding 10^9 A/cm². The rectification of the tunneling junction depends on dc bias voltage, incident THz field, forward or reverse bias, tip-sample separation, local density of states, operating media, and work functions of the tip and sample. In order to achieve better controllability of the tunneling current over ultrafast time scales, enhance rectification of the tip-sample junction, and improve temporal resolution and real-time electron dynamics, basic scaling of the rectified electron current needs to be analyzed in different voltage regimes, for a variety of input parameters.

Recent studies used Simmons formulas for metal-insulator-metal (MIM) junctions [9,16] and Bardeen tunneling model [8,17,18] to fit their THz-STM experimental

*pz@egr.msu.edu

†snebane@sandia.gov

‡Present address: Electrical Models and Simulation, Sandia National Labs, Albuquerque, New Mexico 87123, USA

measurements. Although these models are widely used, they are reliable only in the low-voltage regime where the tunnel junction can be approximated as Ohmic [23,24]. In the nonlinear $I - V$ regime or field emission regime, the effects of space-charge and exchange-correlation potentials, which are ignored in both the Simmons formula [25,26] and Bardeen's theory, become significant. To achieve better characterization of the tip-sample tunneling junction and the THz-induced current transport, a quantum mechanical analysis of the tunneling junction needs to be done.

Here we present a comprehensive study of the ultra-fast electron transport in THz-induced STM junctions. We include the important quantum effects in a tip-vacuum-sample junction and investigate the scaling of the time-dependent tunneling current for a wide range of parameters. We use a self-consistent quantum model [23,24] that includes the effects of space-charge and exchange-correlation potentials, as well as current emission from both tip and sample. We assume that there is no thermal expansion of the tip or sample; the THz-STM is operated in vacuum; the sample surface is flat; and the tip height is fixed. First, we validate our calculation with recently reported experimental data [17,18], then we investigate the rectification of the tip-sample junction for different material properties, barrier heights, tip-sample separations, and bias voltages. We investigate the scaling of tunneling current with respect to several tip-sample junction parameters. Our theoretical calculation assumes that the THz bias voltage $V_{\text{THz}}(t)$ is readily available at the junction and does not examine the generation, propagation, and coupling of the THz pulses to the STM tip. More information on the experimental setup can be found in Refs. [9,17,18] and on

the coupling of THz pulses to the STM tip can be found in Refs. [19,20,27–29].

A brief description of the self-consistent quantum model is presented in Sec. II. Obtained results are discussed in Sec. III. Conclusions and a few aspects of future research are given in Sec. IV.

II. FORMULATION

Terahertz pulses coupled to the STM tip act like fast voltage transients that sample the $I-V$ curve of the tunnel junction with subpicosecond time resolution [9]. The STM tip-vacuum-sample junction is treated as a typical metal-insulator-metal junction [Fig. 1(a)]. The self-consistent model (SCM) formulation is based on our previous works [23,24,30–32]. Although the model used is developed for dc condition, it is demonstrated below to be applicable to THz-STM junctions, since the transit time for electron tunneling through a barrier of nanometer-scale thickness is typically less than 1 fs, much smaller than the period of the THz pulses [33–37]. This means that the tunneling electrons see an approximately constant voltage even though the dc bias is modulated with the THz field, and a simple dc model can be used to analyze the tunneling characteristics of THz-STM.

The potential barrier formed between the STM tip and sample is [Fig. 1(b)] $\Phi(x) = E_F + \Phi_w(x) + \Phi_{\text{image}}(x) + eV(x) + \Phi_{\text{xc}}(x)$, where E_F is the equilibrium Fermi level; $\Phi_w(x) = \phi_t + (\phi_s - \phi_t)x/D$; $\phi_t = W_t - X$; $\phi_s = W_s - X$; W_t and W_s are the work functions of metal tip and sample, respectively; X is the electron affinity of the insulator; $\Phi_{\text{image}}(x)$ is the image charge potential energy including the effect of anode screening [23,24,38]; $eV(x) = eV_g x/D + eV_{\text{sc}}(x)$ is the electric potential, where

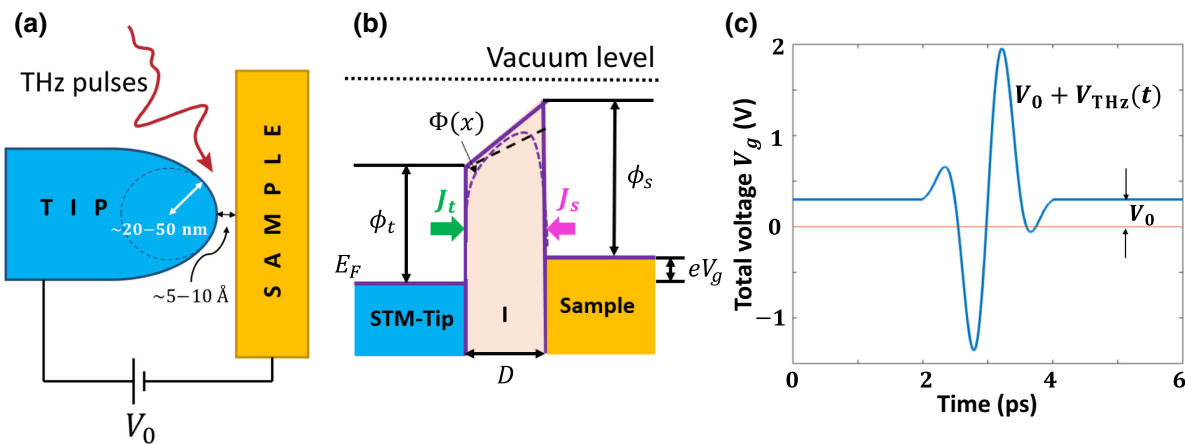


FIG. 1. (a) Schematic diagram of THz-STM on a sample surface. A THz pulse is coupled into the STM junction, inducing transient tunnel currents between the tip and the sample. (b) The potential profile near the tip-sample junction. The tip-sample separation is typically 1–10 Å and the radius of curvature of the tip is 20–50 nm. In (b), $\phi_t = W_t - X$ and $\phi_s = W_s - X$, where W_t and W_s are the work functions of metal tip and sample, respectively, and X is electron affinity of the insulator. J_t and J_s are the electron current densities emitted from the tip and sample, respectively.

V_g is the time-dependent bias voltage [Fig. 1(c)] and $V_{sc}(x)$ is the potential due to space charge; and $\Phi_{xc}(x)$ is the electron exchange-correlation potential calculated by the Kohn-Sham local density approximation [23,24,39].

The probability $D(E_x)$ that an electron with longitudinal energy E_x (normal to the surface) can penetrate the potential barrier $\Phi(x)$ is given by the Wentzel-Kramers-Brillouin-Jeffreys (WKBJ) approximation [40]: $D(E_x) = \exp\left[-2/\hbar \int_{x_1}^{x_2} \sqrt{2m_e[\Phi(x) - E_x]} dx\right]$, where x_1 and x_2 are the two roots of $E_x - \Phi(x) = 0$. The tunneling current densities from tip to sample and from sample to the tip are, respectively [23–25], $J_t = e \int_0^\infty N_t(E_x) D(E_x) dE_x$ and $J_s = e \int_0^\infty N_s(E_x) D(E_x) dE_x$, where $N_t(E_x)$ and $N_s(E_x)$ are the number of electrons inside tip and sample, respectively, with longitudinal energy E_x impinging on the vacuum interface per unit area per unit time, calculated by the free-electron theory of metal [41]. We use $N_t(E_x) = (m_e k_B T / 2\pi^2 \hbar^3) \ln(1 + e^{-(E_x - E_F)/k_B T})$ and $N_s(E_x) = (m_e k_B T / 2\pi^2 \hbar^3) \ln(1 + e^{-(E_x + eV_g - E_F)/k_B T})$, where m_e is the electron rest mass, \hbar is the reduced Planck constant, k_B is the Boltzmann constant, and T is the electrode temperature.

Inside the insulator, $0 < x < D$, we solve the coupled Schrödinger equation and the Poisson equation for the electric potential $eV(x)$ and the exchange-correlation potential $\Phi_{xc}(x)$:

$$-\frac{\hbar^2}{2m_e} \frac{d^2\psi}{dx^2} - [eV(x) - \Phi_{xc}(x)]\psi = E_0\psi, \quad (1)$$

$$\frac{d^2V}{dx^2} = \frac{e\psi\psi^*}{\epsilon_r\epsilon_0}, \quad (2)$$

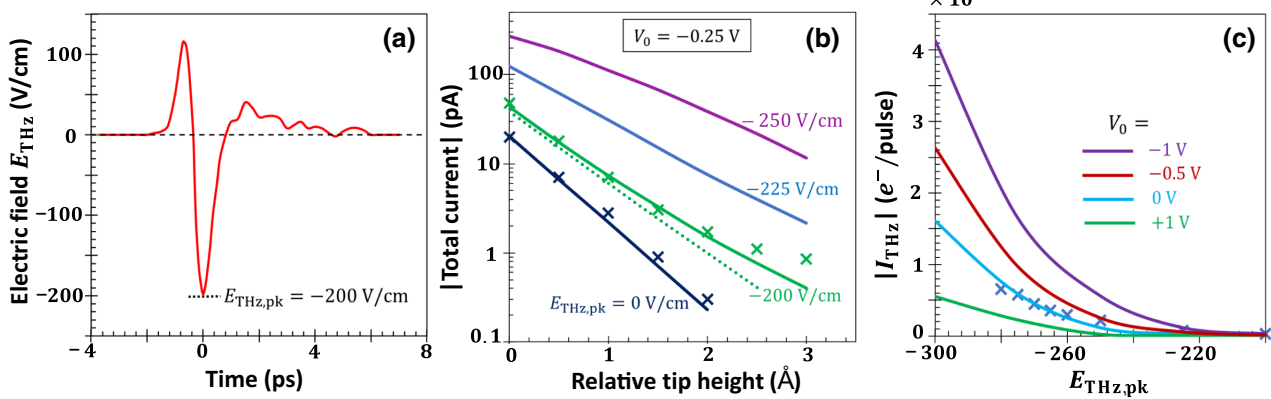


FIG. 2. (a) Terahertz pulse electric field waveform with peak frequency at 0.4 THz [17]. (b) Total current as a function of relative tip height for different peak electric field $E_{THz,pk}$ and a dc bias of -0.25 V. (c) Terahertz-induced current (e^-/pulse) versus peak terahertz electric field (in V/cm) for different dc bias voltages V_0 . The cross symbols are experimental measurements from Ref. [17]. The dotted line in (b) is from Bardeen's tunneling theory [17]. For (b), the initial tip-sample separation $D_0 = 1.12$ nm, which is set by the dc bias $V_0 = -0.25$ V, corresponding to tunneling current $|I_0| = 20$ pA, in the absence of THz field, $E_{THz,pk} = 0$ V/cm. For (c), the tip height maintains $|I_0| = 10$ pA at $V_0 = 1$ V. Here the dc bias is applied to the sample. The material properties and the fitting parameters are specified in the main text.

where ψ is the complex electron wave function, $n = \psi\psi^*$ is the electron density, and E_0 is the electron emission energy (with respect to the Fermi energy E_F). We assume $E_0 = 0$ in the calculation. For a bias voltage V_g , the boundary conditions are $V(0) = 0$ and $V(D) = V_g$. We also have the boundary conditions that both ψ and $d\psi/dx$ are continuous at $x = 0$ and $x = D$. Due to charge conservation, the net current density $J_{\text{net}} = J_t - J_s = e(i\hbar/2m_e)(\psi\psi' - \psi^*\psi')$ is constant for all x , where a prime denotes a derivative with respect to x , and $i = \sqrt{-1}$.

By solving Eqs. (1) and (2) iteratively with the boundary conditions, we can self-consistently obtain the complete potential barrier profile $\Phi(x)$ and the current density emitted from both tip and sample, J_t and J_s , for any W_t , W_s , insulator layer (ϵ_r, X, D), and bias voltage (V_g). It is found that the tunneling current emission is insensitive to the temperature and the Fermi level [24], and in our calculations, we assume room temperature $T = 300$ K and $E_F = 5.53$ eV. The number of electrons generated per pulse is $N = \int_{t_1}^{t_2} I(t) dt/e$, where $I(t)$ is the time-dependent tunneling current through the STM tip, $t_2 - t_1$ is the pulse duration, and e is the electron charge. For a time-dependent V_g , J_{net} is also time-dependent. $I(t)$ is calculated by multiplying J_{net} by the cross-section area of the tip.

III. RESULTS AND DISCUSSION

In Fig. 2 we validate our SCM calculation with experiments [17] and investigate the THz-induced current as functions of tip-to-sample distance (tip height) D and peak electric field $E_{THz,pk}$ of the incident wave. We use experimental measurements reported by Jelic

et al. [17] who performed atomic-resolution imaging of Si(111)–(7 × 7) by focusing asymmetric single-cycle THz pulses (center frequency ∼0.4 THz) on a STM tip. The THz-pulse-induced transient voltage $V_{\text{THz}}(t)$ at the tunneling junction drives a transient tunneling current $I_{\text{THz}}(t)$. $V_{\text{THz}}(t)$ is assumed to have the same temporal profile as $E_{\text{THz}}(t)$. In Fig. 2 we perform a fit for multiple STM and THz-STM measurements. In the self-consistent tunneling model the fitting parameters are barrier height ($\phi_t = \phi_s = 4.8 \pm 0.15$ eV), initial tip-sample separation ($D_0 = 1.0 \pm 0.2$ nm), and terahertz field enhancement ($F = 300\,000 \pm 50\,000$). The time-dependent voltage bias $V_{\text{THz}}(t)$ is calculated from $E_{\text{THz}}(t)$, F , and D using $V_{\text{THz}}(t) = E_{\text{THz}}(t) \times FD$. Here, the tip-to-sample distance D is the sum of D_0 and relative tip height shown in the horizontal axis of Fig. 2(b). The dc bias V_0 generates tunneling current I_0 in the absence of THz field. We assume that the operating medium is ultra-high vacuum with relative permittivity $\epsilon_r = 1$ and electron affinity $X = 0$, the dimension of the area of the STM tip is assumed to be 10 nm × 10 nm, and there is no phase delay between $I_{\text{THz}}(t)$ and $V_{\text{THz}}(t)$. The rectified average tunnel current for the THz component is calculated as $I_{\text{THz,avg}} = 250 \text{ kHz} \times \int I_{\text{THz}}(t) dt$, where the pulse repetition rate is 250 kHz [17,18] and the terahertz-induced current I_{THz} (e^-/pulse) is plotted in Fig. 2(c) as a function of $E_{\text{THz,pk}}$ for different dc bias voltages. For these calculations, bias is applied to the sample. The incident electric field E_{THz} follows the profile shown in Fig. 2(a). The solid lines are from SCM calculation and the cross symbols are from experiments [17]. It is clear that good agreement between the two is obtained. The negative $E_{\text{THz,pk}}$ generates a terahertz-induced rectified current (electrons tunneling from the sample to the tip) at the STM junction when $V_0 = 0$ V. High tunnel current densities (above 10^9 A/cm^2) are observed over a subpicosecond time period that are orders of magnitude higher than the current densities reported for conventional STMs. This is reflected in Fig. 2(b), which shows that the total current for THz-modulated STM is several times higher than the steady-state current for STM [Fig. 2(b); $E_{\text{THz,pk}} = 0 \text{ V/cm}$]. Several experiments [9,17,18,21] reported that these extreme transient currents can be maintained over long periods without damaging the surface or the tip for THz-modulated STMs. Figure 2(b) shows that the total current is extremely sensitive to the tip-sample separation D . It decreases exponentially when D is increased. The terahertz-induced current versus incident peak electric field plot [Fig. 2(c)] demonstrates that a negative dc bias voltage V_0 (to sample) enhances I_{THz} at negative $E_{\text{THz,pk}}$ while a positive V_0 acts oppositely. Due to the highly

nonlinear current-voltage characteristics of the tip-sample tunneling junction, the increase in I_{THz} for $V_0 = -1$ V is much greater than the decrease in I_{THz} for $V_0 = +1$ V [Fig. 2(c)].

Because of the inherent asymmetry and nonlinear I - V characteristics of the tip-sample junction, manipulation of the electron transport over ultrafast time scales becomes possible. The terahertz-driven tunnel current can be controlled by varying the polarity, strength, and asymmetry of the terahertz pulse electric field, work function of the metal tip, polarity and amplitude of the dc bias, and tip-sample separation. It is important to note that the I - V characteristics of a metal-insulator-metal junction can be divided into three distinct regimes [23,24]: (a) direct tunneling regime for low voltages, where the I - V curve is linear and the junction can be approximated as Ohmic, (b) field emission regime for high voltages, where the junction is highly nonlinear and the I - V curve becomes close to the Fowler-Nordheim law [42], and (c) space-charge-limited regime for very high voltages, where it approaches the quantum Child-Langmuir law [43,44]. The THz-STMs are typically operated in the field emission regime [peak $V_g(t) > 1$ V], in order to achieve a high transient tunneling current [peak $I_{\text{THz}}(t) \sim \text{mA}$].

The effects of time-dependent bias voltage $V_g(t) = V_0 + V_{\text{THz}}(t)$ on the ultrafast electron transport are demonstrated in Fig. 3. Figures 3(d)–3(f) show the number of electrons tunneled for different $V_g(t)$ shown in Figs. 3(a)–3(c), respectively. For these calculations, the tip is given a positive bias of 0.3 V and the THz-field-induced voltage $V_{\text{THz}}(t)$ is increased keeping the tip height fixed at 0.5 nm. The work function of both tip and sample is assumed to be $W_s = W_t = 4.5$ eV. The total bias voltage is large enough for the tunneling junction to operate in the field emission regime [23,24]. The total number of electrons tunneled is defined in Sec. II as $N = \int_{t_1}^{t_2} I(t) dt / e$, where $I(t)$ is the time-dependent tunneling current through the STM tip, $t_2 - t_1$ is the duration of interest, and e is the electron charge. The rectangular shape of N profiles represents the total number of electrons tunneled during $t_2 - t_1$, dividing the time axis into four segments. The tunneling current (or the number of electrons per pulse) increases rapidly with the bias. Here, a positive value denotes electron tunneling from sample to tip. These rectified electrons per pulse in a THz-STM can be manipulated by varying the bias voltage (polarity, amplitude) and THz field (polarity, shape, $E_{\text{THz,pk}}$). For example, Figs. 3(a) and 3(d) show that, although the THz-induced transient voltage $V_{\text{THz}}(t)$ is negative for the most part during 2–3 ps, a comparable (with respect to $V_{\text{THz,pk}}$) dc bias voltage drives the net tunneled electrons in the positive direction. On the other hand, Figs. 3(e) and 3(f) show that, if the THz field strength is increased keeping the dc bias fixed, the asymmetry between the positive and negative cycle increases resulting in a better rectification. Note that the shape of $V_{\text{THz}}(t)$

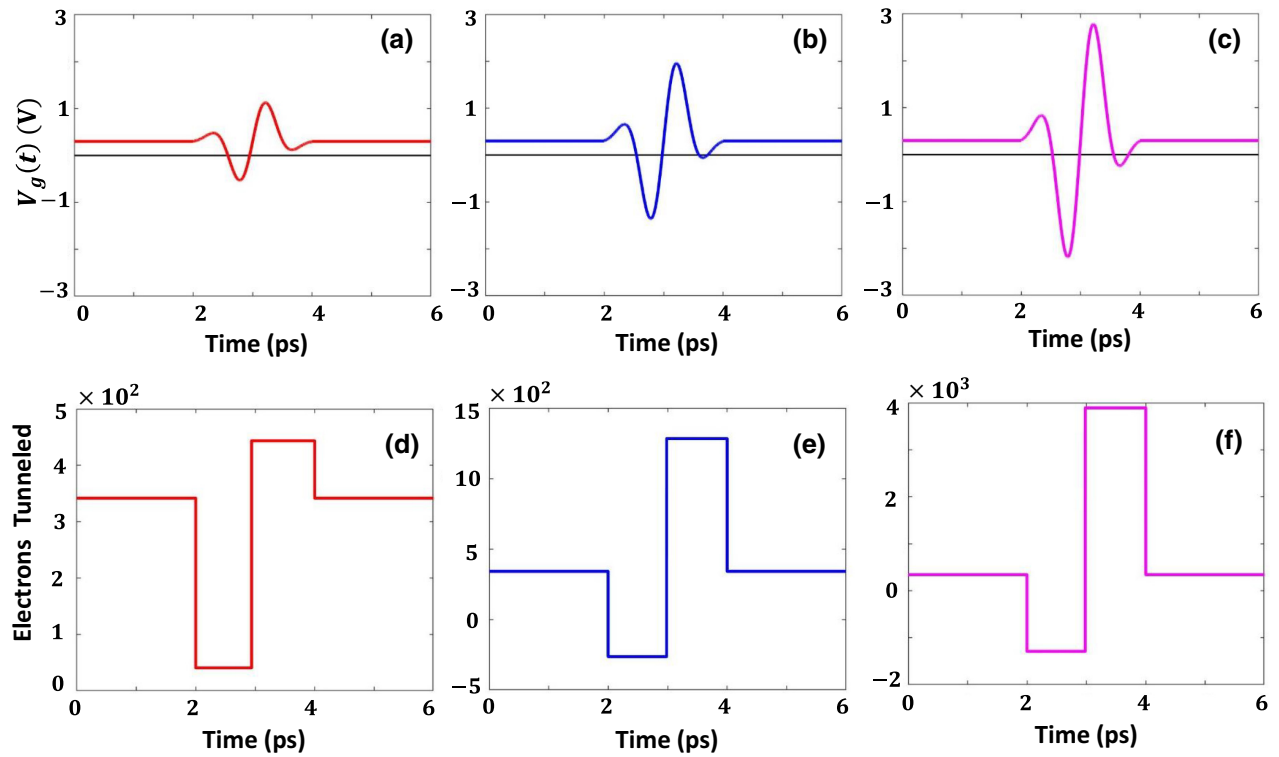


FIG. 3. Effects of time-dependent bias voltage $V_g(t) = V_0 + V_{\text{THz}}(t)$ on the ultrafast electron transport. (a)–(c) Total junction voltages with $V_{g,\text{peak}} = 1.12$, 1.95 and 2.78 V, respectively. A dc bias of $V_0 = 0.3$ V is given to the tip. (d)–(f) Number of electrons tunneled in a THz-STM for tip-vacuum-sample junction with $W_s = W_t = 4.5$ eV for total voltages shown in (a)–(c), respectively. Tip height is 0.5 nm and the THz-STM is operated in vacuum ($\epsilon_r = 1$, $X = 0$ eV).

is important in these studies. If $V_{\text{THz}}(t)$ has a different temporal profile, the results are quite different. For better rectification and enhanced resolution, asymmetric single-cycle $E_{\text{THz}}(t)$ pulses [like in Fig. 2(a)] may be focused on the THz-STM tip.

In Fig. 4 we investigate the time-dependent quantum tunneling current in a THz-STM for a sample having work function $W_s = 4.08$ eV (Al) scanned by different STM probe tips with work functions $W_t = 3$ eV (Ca), 4.5 eV (W), 5.1 eV (Au), and 6.35 eV (Pt). Similar to Fig. 3, we consider that the THz-STM is operated in vacuum ($\epsilon_r = 1$, $X = 0$ eV), the tip is given a positive bias of 0.3 V, and the dimension of the STM tip is 5 nm \times 5 nm. In these calculations, peak THz voltage (4.963 V) and tip height (0.7 nm) are kept fixed. In the absence of THz field, for a dc bias of 0.3 V, the value of $I_0 = 3.0325 \times 10^{-6}$, 4.0065×10^{-6} , 2.0049×10^{-7} , and 5.529×10^{-8} A for Figs. 4(a)–4(d), respectively. Here, the STM tip and sample form an asymmetric metal-insulator-metal junction due to their inherent work function difference. Hence, the tunneling current is dependent on polarity [23,26]. A tunneling junction operates in forward bias (FB) when the electrode with lower work function is positively biased [e.g., Fig. 4(a) with positive V_g at tip] and in reverse bias (RB) when the electrode with higher work

function is given positive bias [e.g., Figs. 4(b)–4(d) with positive V_g at tip]. This asymmetry between the positive and negative periods of $V_{\text{THz}}(t)$ enhances rectification of the tip-vacuum-sample junction and increases with work function difference between tip and sample (Fig. 4). This is because the work function difference $|\Delta W|$ between the two electrodes in a dissimilar MIM junction influences the potential barrier $\Phi(x)$ profoundly [23]. The barrier height lowers significantly with large RB in the field emission regime [23]. The insets in Fig. 4 show the approximate barrier heights between the Al sample and different tips. The actual barriers include image-charge potential, space-charge potential, and exchange-correlation potential and are not sharp-edged trapezoidal in shape as shown in the figure. Here, the insets are drawn only to demonstrate the effects of work function difference on the potential barrier profile and the tunneling characteristics. The top-left insets show a positive $V_g = V_0 + V_{\text{THz}}(t)$ at the tip. The bottom right inset in Fig. 4(a) shows a negative V_g at the tip. In the field emission regime, the tunneling current is significantly higher in the RB condition than the FB condition. That is why the negative peak and the positive peak of the tunneling current in Fig. 4(a) are almost identical even with a dc bias of 0.3 V added to $V_{\text{THz}}(t)$. The reverse bias (positive V_g at tip) barrier heights for $W_t > W_s$ with

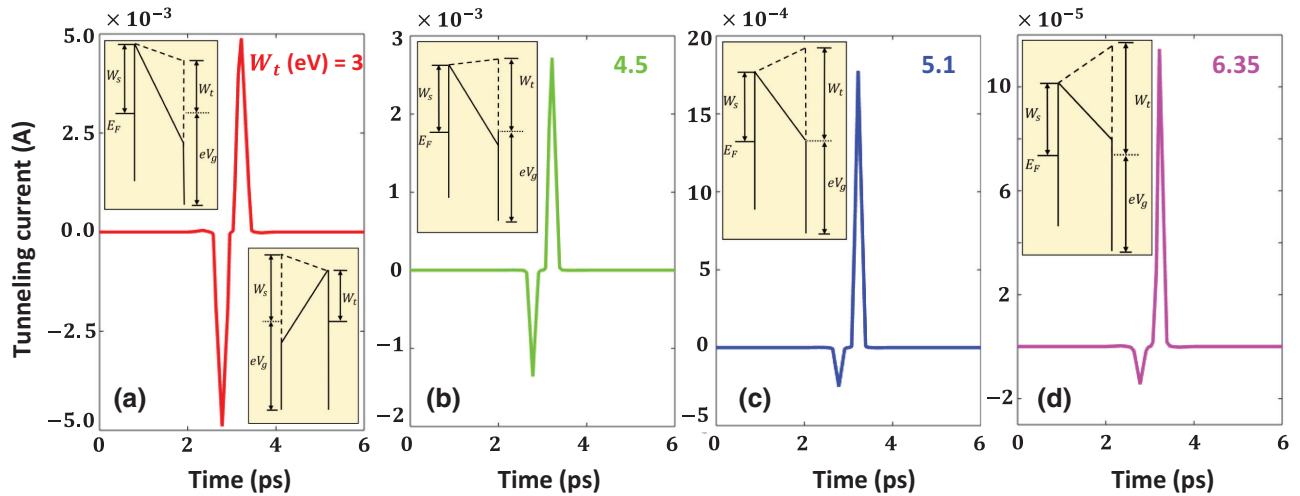


FIG. 4. Time-dependent tunneling current in a THz-STM for a sample having work function $W_s = 4.08$ eV (Al), scanned by tips with work functions W_t = (a) 3 eV (Ca), (b) 4.5 eV (W), (c) 5.1 eV (Au), and (d) 6.35 eV (Pt) in vacuum ($\epsilon_r = 1$, $X = 0$ eV). STM tip is given positive bias of 0.3 V, the peak THz voltage is 4.96 V, and the tip-sample separation is 0.7 nm. The temporal profile of $V_{THz}(t)$ follows Fig. 1(c). Insets at the top-left corners show the approximate barrier between sample and tip during positive $V_g = V_0 + V_{THz}(t)$ at the tip. The bottom-right inset in (a) is for negative V_g at tip.

increasing $\Delta W = |W_t - W_s|$ are shown in the insets of Figs. 4(b)–4(d). The asymmetry of the junction increases with ΔW , resulting in an increased asymmetry in tunneling current between the positive and negative halves of the THz field.

Note that, although the rectification improves when W_t is increased, the peak current reduces since the electrons see a larger barrier. If we want to achieve similar asymmetry without degrading the tunneling current, the Al ($W_s = 4.08$ eV) sample should be scanned with a tip

having lower work function and the polarity of dc bias V_0 should be reversed, that is, positive V_0 should be given to the sample to enhance the reverse bias. The influence of ΔW on the I - V characteristics of a dissimilar MIM junction has been studied thoroughly in Refs. [23,26] for both forward and reverse bias conditions.

In Fig. 5 we study the effects of work function on the ultrafast electron transport of a THz-STM junction and compare the results with the widely used Simmons theory [25,26]. Number of electrons tunneled is plotted as a

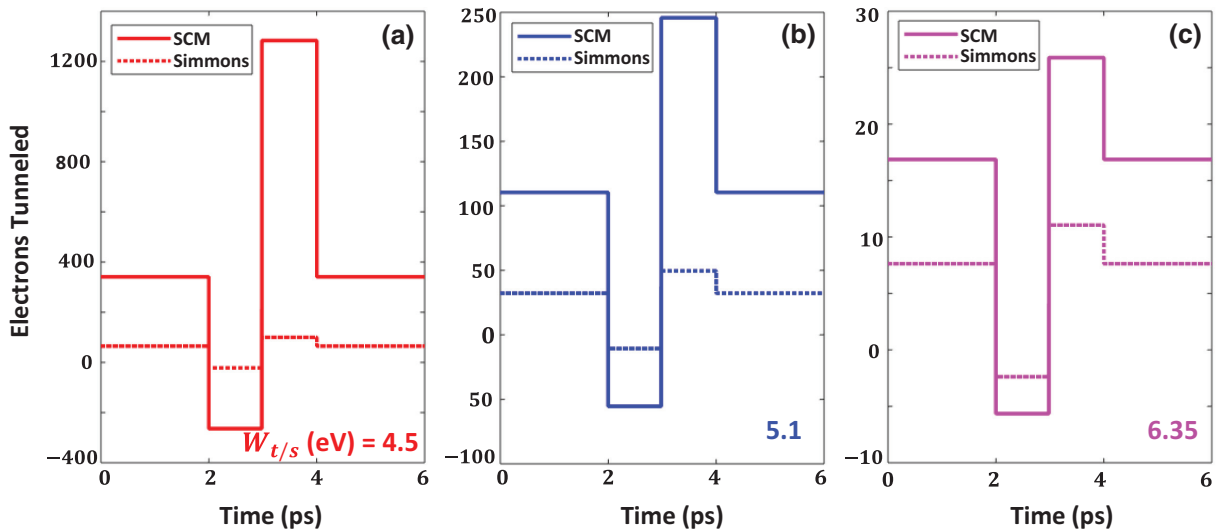


FIG. 5. Number of electrons tunneled in a THz-STM for tip-vacuum-sample junction with $W_s = W_t$ = (a) 4.5 eV (W), (b) 5.1 eV (Au), and (c) 6.35 eV (Pt). Tip height is 0.5 nm and the THz-STM is operated in vacuum ($\epsilon_r = 1$, $X = 0$ eV). STM tip is given a positive bias of 0.3 V and the peak THz voltage is 1.655 V. Solid and dotted lines are for calculations from SCM and the Simmons formula [25], respectively. The temporal profile of $V_{THz}(t)$ follows Fig. 1(c).

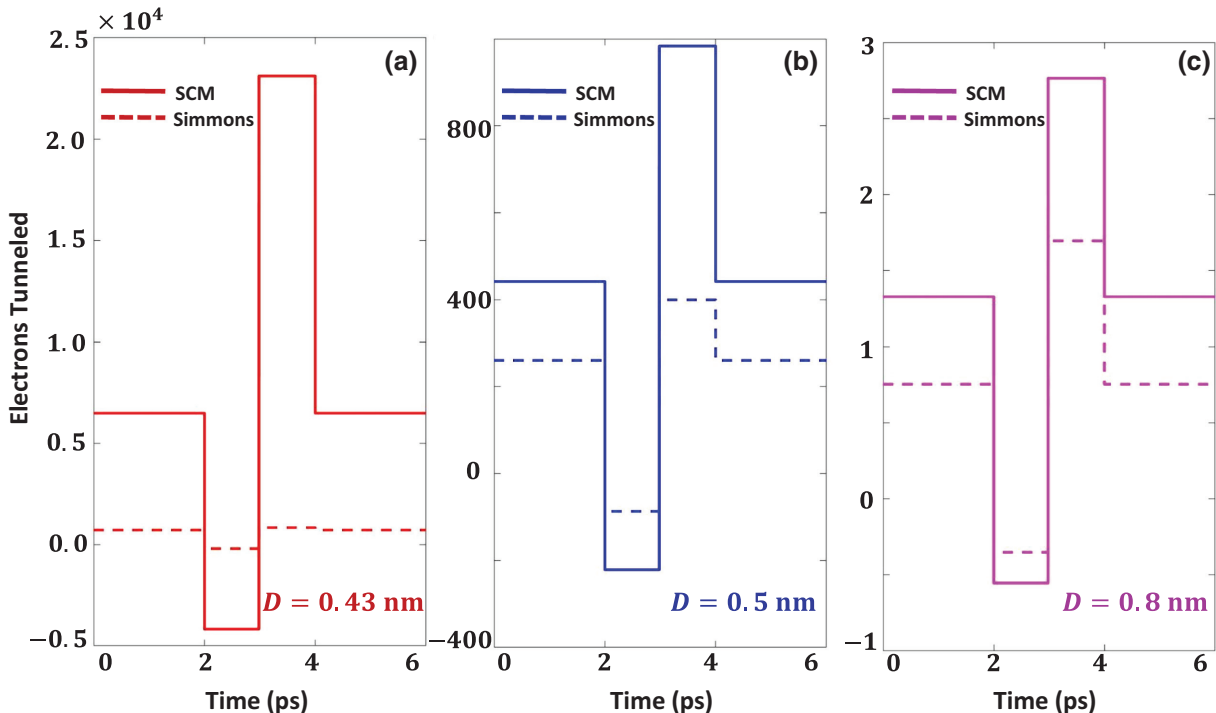


FIG. 6. Number of electrons tunneled in a THz-STM for tip-vacuum-sample junctions with $W_s = W_t = 4.5$ eV and $D =$ (a) 0.43 nm, (b) 0.5 nm, and (c) 0.8 nm. The THz-STM is operated in vacuum ($\epsilon_r = 1$, $X = 0$ eV). STM tip is given a positive bias of 0.3 V and the peak THz voltage is 1.655 V. Solid and dashed lines are for calculations from SCM and the Simmons formula [25], respectively. The temporal profile of $V_{\text{THz}}(t)$ follows Fig. 1(c). The area dimension of the STM tip is 10 nm \times 10 nm.

function of time for various tip-vacuum-sample junctions with $W_s = W_t = 4.5$ eV (W), 5.1 eV (Au), and 6.35 eV (Pt). The THz-STM is operated in vacuum ($\epsilon_r = 1$, $X = 0$ eV) and the tip is given a positive bias of 0.3 V. The tip height is 0.5 nm and the peak THz voltage is 1.655 V. From Fig. 5 we see that the number of tunneled electrons increases with decreasing work function. The potential barrier at the tip-vacuum-sample junction becomes lower when the tunneling junction is formed between materials with lower work function. We also see that the difference between SCM calculation and Simmons formula increases with decreasing work function (Fig. 5). The underlying reason is that the influence of exchange-correlation potential [39], which is ignored in the Simmons formula, is profound in the field emission voltage regime [23,24] where the THz-STMs are generally operated. This exchange-correlation potential reduces the potential barrier and increases the electron tunneling probability. Hence, Simmons formulas are not reliable for modeling ultrafast STMs; the quantum analysis of the tunneling junction using our SCM may give a more accurate estimation of the time-dependent electron transport.

In Fig. 6 we study the effects of tip-sample separation D on the ultrafast electron transport of a THz-STM and compare the results with the Simmons theory. Number of electrons tunneled is plotted over a pulse duration

for various tip heights, $D = 0.43$, 0.5, and 0.8 nm. The work function of both tip and sample is assumed to be $W_s = W_t = 4.5$ eV and the area dimension of the STM tip is assumed to be 10 nm \times 10 nm. The tip is given a positive bias of 0.3 V and the peak THz voltage is 1.655 V. We see that the tunneling current depends sensitively on the tip height D . The number of tunneled electrons increases significantly even when the tip height is decreased slightly. This is quite common in a typical MIM tunneling junction, where the quantum tunneling current increases exponentially with decreasing insulator thickness [17,18,21,23–26]. Figure 6 also indicates that the difference between quantum SCM calculation and the Simmons formula increases with decreasing tip height. This trend is expected since the effects of exchange-correlation potential, which are ignored in the Simmons formula, increase as tip height decreases [44,45].

IV. SUMMARY

We present a theoretical study of ultrafast current transport at THz-STM junctions using a quantum mechanical self-consistent model [23,24]. First, we validate our calculation with recently reported experimental data [17,18], and then we investigate the rectification property of the

tip-sample junction for different material properties, barrier heights, tip-sample separations, and bias voltages. We observe extreme THz-pulse-induced current densities (greater than 10^9 A/cm^2). We find that Simmons formulas [25,26] are not reliable for modeling ultrafast STMs since they operate in the tunneling field emission regime where the effects of exchange-correlation potential become important. We also find that current transport in ultrafast THz-STMs greatly depends on the dc bias voltage (polarity, amplitude), incident THz field (polarity, shape, $E_{\text{THz},\text{pk}}$), work functions of STM tip and sample (especially their difference ΔW), and tip-sample separation. The number of tunneled electrons increases when the THz field increases or the tip height decreases. In dissimilar tip-vacuum-sample junction, quantum tunneling current is dependent on polarity and the junction is asymmetric. This asymmetry between positive and negative halves increases with the work function difference. Better rectification can be obtained when the tip-vacuum-sample junction is operated under reverse bias [23,26], that is, the higher-work-function material is given a large positive bias. This study provides a framework for understanding the scaling of THz-induced currents in a THz-STM junction system, opening the door for manipulation of the time-dependent tunneling current.

In this formulation, we assume that the electron transmission probability during the emission process can be approximated by the WKBJ solution, where the metal electrodes are based on the free electron gas model. Although widely used, both the free electron gas model assumption and the WKBJ approximation need to be examined in future. The time-independent Schrödinger equation may be solved numerically to get a more accurate description of the transmission probability. Furthermore, we consider the tip and sample surface to be flat and the problem is one-dimensional, which may not be the case in practice [17,18]. The effects of their geometry may be included in future works. Terahertz pulse coupling to an STM junction, the corresponding asymmetric field enhancement [46], and subwavelength confinement [47] may also be included in future studies, perhaps using the concepts of antenna theory [19,20,28,48]. We assume both tip and sample to be metals in this study. In the future, semiconductor sample surfaces may be considered. Hence, ultrafast terahertz-induced band bending and nonequilibrium charging of the surface states may be investigated.

In this work, we argue that the electron tunneling time is negligible compared with the time period of the THz field [16,33,35,49] and our solution of the time-independent Schrödinger equation can provide basic scaling of the tunneling current and rectification at the tip-sample junction. However, in order to study the electron dynamics on an ultrafast time scale and to accurately account for the temporal dependencies of the nanoscale system, time-dependent analysis of the electron wave

function may be performed. State-of-the-art methods used for these kinds of studies include the time-dependent density functional theory [50–52], the time-dependent density matrix model [53–55], and the direct solution of the time-dependent Schrödinger equation [56–59]. In the future, a thorough analysis of the time-dependent studies may be done to compare with our results and define regimes where the proposed simple dc model becomes inapplicable.

Finally, it is worth pointing out that our models and results for the quantum tunneling current under ultrafast bias may also be beneficial to a variety of other applications beyond THz-STM junctions, including ultrafast and nanoscale diodes [60–62], ultrafast electron emitters [56,57], quantum plasmonic dimers [24,38], ultrafast photodetectors [24,63], and nanoscale electrical contacts [30, 31,64–68] and junctions in advanced nanoelectronics [63]. Future work may also identify the regime in which the dc models adapted in this work become invalid such that the theory of quantum tunneling current under oscillating bias [56] has to be used.

ACKNOWLEDGMENTS

This work is supported by Air Force Office of Scientific Research (AFOSR) YIP Grant No. FA9550-18-1-0061 and Sandia's 01355 Electrical Models and Simulation group. Sandia National Laboratories is a multimission laboratory managed and operated by National Technology and Engineering Solutions of Sandia, LLC, a wholly owned subsidiary of Honeywell International Inc., for the U.S. Department of Energy's National Nuclear Security Administration under Contract No. DE-NA0003525.

CONFLICTS OF INTEREST

The authors declare no competing financial interest.

-
- [1] M. Razavy, *Quantum theory of tunneling* (World Scientific, River Edge, NJ, 2003).
 - [2] *Scanning Tunneling Microscopy*, edited by H. Neddermeyer (Springer Netherlands, 1993).
 - [3] G. Binnig and H. Rohrer, Scanning tunneling microscopy, *Surf. Sci.* **126**, 236 (1983).
 - [4] G. Binnig, H. Rohrer, Ch. Gerber, and E. Weibel, Surface Studies by Scanning Tunneling Microscopy, *Phys. Rev. Lett.* **49**, 57 (1982).
 - [5] J. Tersoff and D. R. Hamann, Theory of the scanning tunneling microscope, *Phys. Rev. B* **31**, 805 (1985).
 - [6] F. Besenbacher, E. Lægsgaard, and I. Stensgaard, Fast-scanning STM studies, *Mater. Today* **8**, 26 (2005).
 - [7] S. Uemura, R. Tanoue, N. Yilmaz, A. Ohira, and M. Kunitake, Molecular dynamics in two-dimensional supramolecular systems observed by STM, *Materials* **3**, 4252 (2010).
 - [8] T. L. Cocker, D. Peller, P. Yu, J. Repp, and R. Huber, Tracking the ultrafast motion of a single molecule by femtosecond orbital imaging, *Nature* **539**, 263 (2016).

- [9] T. L. Cocker, V. Jelic, M. Gupta, S. J. Molesky, J. A. J. Burgess, G. D. L. Reyes, L. V. Titova, Y. Y. Tsui, M. R. Freeman, and F. A. Hegmann, An ultrafast terahertz scanning tunnelling microscope, *Nat. Photonics* **7**, 620 (2013).
- [10] N. N. Khusnatdinov, T. J. Nagle, and G. Nunes, Ultrafast scanning tunneling microscopy with 1 nm resolution, *Appl. Phys. Lett.* **77**, 4434 (2000).
- [11] K. Iwaszczuk, M. Zalkovskij, A. C. Strikwerda, and P. U. Jepsen, Nitrogen plasma formation through terahertz-induced ultrafast electron field emission, *Optica* **2**, 116 (2015).
- [12] V. Jelic, K. Iwaszczuk, P. H. Nguyen, C. Rathje, G. J. Hornig, H. M. Sharum, J. R. Hoffman, M. R. Freeman, and F. A. Hegmann, *Frontiers in Optics* (2016), Paper FF3F.2 (Optical Society of America, New York, United States, 2016), pp. FF3F.2.
- [13] Y. Terada, S. Yoshida, O. Takeuchi, and H. Shigekawa, Real-space imaging of transient carrier dynamics by nanoscale pump-probe microscopy, *Nat. Photonics* **4**, 869 (2010).
- [14] S. Yoshida, Y. Terada, R. Oshima, O. Takeuchi, and H. Shigekawa, Nanoscale probing of transient carrier dynamics modulated in a GaAs-PIN junction by laser-combined scanning tunneling microscopy, *Nanoscale* **4**, 757 (2012).
- [15] G. M. Steeves, A. Y. Elezzabi, and M. R. Freeman, Nanometer-scale imaging with an ultrafast scanning tunneling microscope, *Appl. Phys. Lett.* **72**, 504 (1998).
- [16] K. Yoshioka, I. Katayama, Y. Arashida, A. Ban, Y. Kawada, H. Takahashi, and J. Takeda, Sub-cycle manipulation of electrons in a tunnel junction with phase-controlled single-cycle THz near-fields, *EPJ Web Conf.* **205**, 08007 (2019).
- [17] V. Jelic, K. Iwaszczuk, P. H. Nguyen, C. Rathje, G. J. Hornig, H. M. Sharum, J. R. Hoffman, M. R. Freeman, and F. A. Hegmann, Ultrafast terahertz control of extreme tunnel currents through single atoms on a silicon surface, *Nat. Phys.* **13**, 591 (2017).
- [18] Y. Luo, V. Jelic, G. Chen, P. H. Nguyen, Y.-J. R. Liu, J. A. M. Calzada, D. J. Mildenberger, and F. A. Hegmann, Nanoscale terahertz STM imaging of a metal surface, *Phys. Rev. B* **102**, 205417 (2020).
- [19] K. Wang, D. M. Mittleman, N. C. J. van der Valk, and P. C. M. Planken, Antenna effects in terahertz apertureless near-field optical microscopy, *Appl. Phys. Lett.* **85**, 2715 (2004).
- [20] M. Walther, G. S. Chambers, Z. Liu, M. R. Freeman, and F. A. Hegmann, Emission and detection of terahertz pulses from a metal-tip antenna, *J. Opt. Soc. Am. B* **22**, 2357 (2005).
- [21] M. Müller, N. Martín Sabanés, T. Kampfrath, and M. Wolf, Phase-resolved detection of ultrabroadband THz pulses inside a scanning tunneling microscope junction, *ACS Photonics* **7**, 2046 (2020).
- [22] T. Tachizaki, K. Hayashi, Y. Kanemitsu, and H. Hirori, On the progress of ultrafast time-resolved THz scanning tunneling microscopy, *APL Mater.* **9**, 060903 (2021).
- [23] S. Banerjee and P. Zhang, A generalized self-consistent model for quantum tunneling current in dissimilar metal-insulator-metal junction, *AIP Adv.* **9**, 085302 (2019).
- [24] P. Zhang, Scaling for quantum tunneling current in nano- and subnano-scale plasmonic junctions, *Sci. Rep.* **5**, 9826 (2015).
- [25] J. G. Simmons, Generalized formula for the electric tunnel effect between similar electrodes separated by a thin insulating film, *J. Appl. Phys.* **34**, 1793 (1963).
- [26] J. G. Simmons, Electric tunnel effect between dissimilar electrodes separated by a thin insulating film, *J. Appl. Phys.* **34**, 2581 (1963).
- [27] K. Wang and D. M. Mittleman, Metal wires for terahertz wave guiding, *Nature* **432**, 7015 (2004).
- [28] J. A. Deibel, K. Wang, M. Escarra, N. Berndsen, and D. M. Mittleman, The excitation and emission of terahertz surface plasmon polaritons on metal wire waveguides, *C. R. Phys.* **9**, 215 (2008).
- [29] A. J. Adam, N. C. van der Valk, and P. C. Planken, Measurement and calculation of the near field of a terahertz apertureless scanning optical microscope, *J. Opt. Soc. Am. B* **24**, 1080 (2007).
- [30] S. Banerjee, P. Y. Wong, and P. Zhang, Contact resistance and current crowding in tunneling type circular nano-contacts, *J. Phys. D: Appl. Phys.* **53**, 355301 (2020).
- [31] S. Banerjee, J. Luginsland, and P. Zhang, Interface Engineering of Electrical Contacts, *Phys. Rev. Appl.* **15**, 064048 (2021).
- [32] S. Banerjee, Doctoral Thesis, Michigan State University ProQuest Dissertations Publishing, 2021.
- [33] P. Février and J. Gabelli, Tunneling time probed by quantum shot noise, *Nat. Commun.* **9**, 4940 (2018).
- [34] M. Uiberacker, Th. Uphues, M. Schultze, A. J. Verhoef, V. Yakovlev, M. F. Kling, J. Rauschenberger, N. M. Kabachnik, H. Schröder, M. Lezius, *et al.*, Attosecond real-time observation of electron tunnelling in atoms, *Nature* **446**, 627 (2007).
- [35] G. Nimtz, Tunneling confronts special relativity, *Found. Phys.* **41**, 1193 (2011).
- [36] K. K. Thornber, T. C. McGill, and C. A. Mead, The tunneling time of an electron, *J. Appl. Phys.* **38**, 2384 (1967).
- [37] K. L. Jensen, A. Shabaev, J. Riga, D. A. Shiffler, J. L. Lebowitz, and R. Sevior, Reevaluating the Hartman effect for field emission, *Phys. Rev. A* **104**, 062203 (2021).
- [38] L. Wu, H. Duan, P. Bai, M. Bosman, J. K. W. Yang, and E. Li, Fowler-Nordheim tunneling induced charge transfer plasmons between nearly touching nanoparticles, *ACS Nano* **7**, 707 (2013).
- [39] J. P. Perdew and Y. Wang, Accurate and simple analytic representation of the electron-gas correlation energy, *Phys. Rev. B* **45**, 13244 (1992).
- [40] David Bohm, *Quantum Theory* (Prentice-Hall, New York, 1952).
- [41] M. Ali Omar, *Elementary Solid State Physics* (Pearson, New Delhi, 2008).
- [42] R. H. Fowler and L. Nordheim, Electron emission in intense electric fields, *Proc. R. Soc. A* **119**, 173 (1928).
- [43] Y. Y. Lau, D. Chernin, D. G. Colombant, and P.-T. Ho, Quantum Extension of Child-Langmuir Law, *Phys. Rev. Lett.* **66**, 1446 (1991).

- [44] L. K. Ang, T. J. T. Kwan, and Y. Y. Lau, New Scaling of Child-Langmuir Law in the Quantum Regime, *Phys. Rev. Lett.* **91**, 208303 (2003).
- [45] L. K. Ang, Y. Y. Lau, and T. J. T. Kwan, Simple derivation of quantum scaling in Child-Langmuir law, *IEEE Trans. Plasma Sci.* **32**, 410 (2004).
- [46] J. Lin, P. Y. Wong, P. Yang, Y. Y. Lau, W. Tang, and P. Zhang, Electric field distribution and current emission in a miniaturized geometrical diode, *J. Appl. Phys.* **121**, 244301 (2017).
- [47] X. Xiong, Y. Zhou, Y. Luo, X. Li, M. Bosman, L. K. Ang, P. Zhang, and L. Wu, Plasmon-enhanced resonant photoemission using atomically thick dielectric coatings, *ACS Nano* **14**, 8806 (2020).
- [48] K. Yoshida, K. Shibata, and K. Hirakawa, Terahertz Field Enhancement and Photon-Assisted Tunneling in Single-Molecule Transistors, *Phys. Rev. Lett.* **115**, 138302 (2015).
- [49] G. Nimtz and H. Aichmann, All waves have a zero tunneling time, *Z. Für Naturforschung A* **76**, 295 (2021).
- [50] D. Kidd, X. Xu, C. Covington, K. Watanabe, and K. Varga, Simulation of laser-induced rectification in a nano-scale diode, *J. Appl. Phys.* **123**, 054501 (2018).
- [51] K. Uchida and K. Watanabe, Plasmon excitation and electron emission of a carbon nanotube under a linearly polarized laser: A real-time first-principles study, *Phys. Rev. B* **96**, 125419 (2017).
- [52] M. Ludwig, A. K. Kazansky, G. Aguirregabiria, D. C. Marinica, M. Falk, A. Leitenstorfer, D. Brida, J. Aizpurua, and A. G. Borisov, Active control of ultrafast electron dynamics in plasmonic gaps using an applied bias, *Phys. Rev. B* **101**, 241412 (2020).
- [53] A. T. Georges and N. E. Karatzas, Modeling of ultrafast interferometric three-photon photoemission from a metal surface irradiated with sub-10-fs laser pulses, *Phys. Rev. B* **77**, 085436 (2008).
- [54] N. E. Karatzas and A. T. Georges, Model for ultrafast harmonic generation from a gold surface: Extraction of dephasing times for continuum-continuum transitions, *J. Opt. Soc. Am. B* **26**, 2218 (2009).
- [55] H. Ueba and B. Gumhalter, Theory of two-photon photoemission spectroscopy of surfaces, *Prog. Surf. Sci.* **82**, 193 (2007).
- [56] Y. Luo and P. Zhang, Ultrafast optical-field-induced photo-electron emission in a vacuum nanoscale gap: An exact analytical formulation, *Appl. Phys. Lett.* **119**, 194101 (2021).
- [57] Y. Luo, Y. Zhou, and P. Zhang, Few-cycle optical-field-induced photoemission from biased surfaces: An exact quantum theory, *Phys. Rev. B* **103**, 085410 (2021).
- [58] Y. Luo and P. Zhang, Optical-Field-Induced Electron Emission in a Dc-Biased Nanogap, *Phys. Rev. Appl.* **17**, 044008 (2022).
- [59] G. Z. Kiss, P. Földi, and P. Dombi, Ultrafast plasmonic photoemission in the single-cycle and few-cycle regimes, *Sci. Rep.* **12**, 1 (2022).
- [60] P. Zhang and Y. Y. Lau, Ultrafast and nanoscale diodes, *J. Plasma Phys.* **82**, 595820505 (2016).
- [61] P. Zhang, Á. Valfells, L. K. Ang, J. W. Luginsland, and Y. Y. Lau, 100 years of the physics of diodes, *Appl. Phys. Rev.* **4**, 011304 (2017).
- [62] P. Zhang, Y. S. Ang, A. L. Garner, Á. Valfells, J. W. Luginsland, and L. K. Ang, Space-charge limited current in nanodiodes: Ballistic, collisional, and dynamical effects, *J. Appl. Phys.* **129**, 100902 (2021).
- [63] L. Chen, S. Mao, P. Wang, Z. Yao, Z. Du, Z. Zhu, L. A. Belfiore, and J. Tang, Visible light driven hot-electron injection by Pd nanoparticles: Fast response in metal–semiconductor photodetection, *Adv. Opt. Mater.* **9**, 2001505 (2021).
- [64] S. Banerjee, J. Luginsland, and P. Zhang, A two dimensional tunneling resistance transmission line model for nanoscale parallel electrical contacts, *Sci. Rep.* **9**, 14484 (2019).
- [65] S. Banerjee, L. Cao, Y. S. Ang, L. K. Ang, and P. Zhang, Reducing Contact Resistance in Two-Dimensional-Material-Based Electrical Contacts by Roughness Engineering, *Phys. Rev. Appl.* **13**, 064021 (2020).
- [66] P. Yang, S. Banerjee, W. Kuang, Y. Ding, Q. Ma, and P. Zhang, Current crowding and spreading resistance of electrical contacts with irregular contact edges, *J. Phys. Appl. Phys.* **53**, 485303 (2020).
- [67] S. Banerjee and P. Zhang, Review of recent studies on nanoscale electrical junctions and contacts: Quantum tunneling, current crowding, and interface engineering, *J. Vac. Sci. Technol., A* **40**, 030802 (2022).
- [68] P. Zhang, S. Banerjee, and J. Luginsland, “Tunneling Electrical Contacts,” Patent US 10,755,975 B2, Aug. 25, 2020.